Chemical Science

ROYAL SOCIETY OF CHEMISTRY

EDGE ARTICLE

View Article Online
View Journal | View Issue

Cite this: *Chem. Sci.*, 2024, **15**, 13218

All publication charges for this article have been paid for by the Royal Society of Chemistry

Received 8th May 2024
Accepted 17th July 2024

DOI: 10.1039/d4sc03023k

rsc.li/chemical-science

Deciphering charge transfer dynamics of a lead halide perovskite–nickel(II) complex for visible light photoredox C–N coupling†

Vishesh Kumar,[a] Sunil Kumar Patel,[b] Ved Vyas,[a] Deepak Kumar,[a] E. Siva Subramaniam Iyer *[b] and Arindam Indra *[a]

Photoredox catalysis involving perovskite quantum dots (QDs) has gained enormous attention because of their high efficiency and selectivity. In this study, we have demonstrated $CsPbBr_3$ QDs as photocatalysts for the C–N bond formation reaction. The introduction of $Ni(dmgH)_2$ (dmgH = dimethyl glyoximato) as a cocatalyst with $CsPbBr_3$ QDs facilitates photocatalytic C–N coupling to form a wide variety of amides. The optimized interaction between the cocatalyst and photocatalyst enhances charge transfer and mitigates charge recombination, ultimately boosting photocatalytic performance. The photocatalytic activity is notably influenced by the variation in the amount of cocatalyst and 7 wt% $Ni(dmgH)_2$ produces the best yield (92%) of amide. Femtosecond transient absorption spectroscopy reveals that the dynamics of the trap states of QDs are affected by cocatalyst. Further, $Ni(dmgH)_2$ facilitates molecular oxygen activation to form superoxide radicals, which further initiates the radical pathway for the C–N coupling.

Introduction

Visible light-driven photoredox catalysis has been widely explored as a versatile and effective platform for the synthesis of different organic compounds.[1–3] When exposed to visible light, semiconductor photocatalysts undergo a redistribution of surface electron clouds, triggered by the excitation of electrons from the valence band (VB) to the conduction band (CB).[4–8] This photophysical process leads to the concurrent generation of both reducing and oxidizing centers on the photocatalyst surface.[9,10] The photogenerated electrons and holes with the appropriate lifetimes are efficiently transported to the catalytic sites to initiate the redox processes.[11–13]

In this context, $CsPbBr_3$ QDs have been explored as the photoredox catalyst for various organic reactions.[14,15] The kinetic energy associated with the CB electrons of QDs and the favorable reduction potential enable them to overcome the energy barriers and facilitate charge transfer, ultimately favoring photocatalytic activity. High light-absorption efficiency, low exciton binding energy, high carrier mobility, and optimized electron–hole diffusion length make them ideal for photoredox catalysis.[16,17] Further, the long-lived active carriers of $CsPbBr_3$ QDs promote photocatalytic organic reactions.[18]

For example, $CsPbBr_3$ QDs have been employed to selectively oxidize benzyl alcohols to benzaldehydes under visible light irradiation.[19] Similarly, photoredox catalysis of $CsPbBr_3$ QDs has been explored for the oxidative coupling of thiols to disulfides, cross-coupling of phosphonates with tertiary amines, α-alkylation of aldehydes, *etc.*[20] Recently, Yan groups explored the photoredox properties of $CsPbBr_3$ QDs for organic transformation reactions such as C–C, C–O, and C–N coupling reactions.[21] $CsPbBr_3$ QDs have been also explored by other groups for facilitating coupling reactions including C–C,[22,23] N–N,[24] C–S,[25] or C–P[25] bond formation processes.

On the other hand, the photocatalytic production of amide by the reaction of aldehyde and amine has been explored by different groups.[26,27] Amides serve as the foundational components of natural peptides and crucial intermediates in the production of polymers, agrochemicals, and pharmaceuticals.[27–30] While simple, the traditional thermal condensation of carboxylic acids and amines is limited to substrate scope because of the harsh reaction conditions.[31] Similarly, traditional approaches involving derivatives of activated carboxylic acids and amines, such as the Beckmann rearrangement, Schmidt and Staudinger reaction often result in a substantial waste production.[32] This ongoing challenge of achieving efficient amide synthesis while minimizing waste has prompted the exploration of novel photocatalytic strategies from both industrial and academic standpoints.

However, most of the photochemical methods for amide synthesis in the homogeneous medium suffer from drawbacks

[a]*Department of Chemistry, Indian Institute of Technology (BHU), Varanasi, 221005, UP, India. E-mail: arindam.chy@iitbhu.ac.in*

[b]*School of Chemical and Materials Sciences, Indian Institute of Technology Goa, Ponda, Goa, India. E-mail: essiyer@iitgoa.ac.in*

† Electronic supplementary information (ESI) available: Experimental details, including synthesis, characterization, spectroscopic and photoelectrochemical measurement, characterization, catalytic studies, ^1H NMR, and ^{13}C NMR spectroscopy. See DOI: https://doi.org/10.1039/d4sc03023k

like costly catalysts, use of non-oxygen oxidizing agents, and limited tolerance towards secondary amines. Simpler methodologies using photocatalysts like phenazine salt, Rose Bengal, and aminoanthraquinone derivatives were found to be promising.[26] Further, heterogeneous photoredox catalysts (Ag/g-C_3N_4, Ni/g-C_3N_4, Ag_2O/P–C_3N_4, TiO_2, and Fe_3O_4/PDA/CdS) have been demonstrated for oxidative amination of aldehydes.[26]

In this context, we have explored the photoredox properties of $CsPbBr_3$ QDs for the formation of a series of structurally versatile amides by the reaction of aldehydes and amines. To improve the charge transfer dynamics and access catalytic active sites, $[Ni(dmgH)_2]$ was used as the cocatalyst with $CsPbBr_3$ QDs. The combination of $[Ni(dmgH)_2]$ and $CsPbBr_3$ produced high efficiency for the oxidative C–N bond formation by the reaction of secondary amines and aldehydes to form structurally diverse amides (highest yield = 92%). The catalyst can be recycled four times with a minimum loss of initial activity. Further, the transient absorption spectroscopic studies have revealed that $[Ni(dmgH)_2]$ acts as an electron funnel, enabling fast electron transfer from QDs to the catalytic centers.

Results and discussion

Syntheses and characterizations of the catalysts

Metal halide perovskite $CsPbBr_3$ QDs were synthesized by hot-injection method following a literature report (Experimental†).[33] The powder X-ray diffraction (PXRD) revealed the monoclinic crystal structure of $CsPbBr_3$ QDs (JCPDS card no. 18-0364) (Fig. S1a and b†).[33,34] The transmission electron microscopy (TEM) study revealed the average particle size as 5.5 ± 1 nm (Fig. S1c†). HRTEM detected the lattice spacing corresponding to (200), (210), (202), (211), and (002) planes of monoclinic $CsPbBr_3$ (Fig. S1c–e†).[35,36] The energy-dispersive X-ray (EDX) spectroscopy confirmed the presence of the elements Cs, Pb, and Br (Fig. S2†). For the photoredox reaction, $[Ni(dmgH)_2]$ was used as the cocatalyst to improve the efficiency and selectivity of the reaction. The addition of different weight% of $[Ni(dmgH)_2]$ (3, 5, 7, and 9 wt%) into the reaction mixture showed a significant variation in the photocatalytic activity (Table S1†) (see later). Therefore, we have carried out a detailed optoelectronic characterization of the catalyst systems having different amounts of $[Ni(dmgH)_2]$ with $CsPbBr_3$ QDs. The UV-visible diffuse reflectance spectroscopy (DRS) revealed the bandgap of $CsPbBr_3$ QDs as 2.28 eV and the addition of $[Ni(dmgH)_2]$ did not alter the bandgap of the photocatalyst (Fig. S3a and b†).[37] However, a broad peak for ligand-to-metal charge transfer (LMCT) in $[Ni(dmgH)_2]$ was detected after the introduction of the cocatalyst to $CsPbBr_3$ (Fig. S3a†).[38] The absorption maxima was shifted to lower wavelength (blue shift) due to the electronic interaction of $[Ni(dmgH)_2]$ with $CsPbBr_3$ QDs.

In Mott–Schottky (MS) plot, both $CsPbBr_3$ QDs and $[Ni(dmgH)_2]$ exhibited positive slopes within the frequency range of 0.5–1.5 kHz, signifying the formation of an n–n-type heterojunction. Based on MS plots, we have determined the flat band potentials as −0.99 eV and −0.59 eV *vs.* NHE (normal hydrogen electrode) for $CsPbBr_3$ and $[Ni(dmgH)_2]$, respectively (Fig. 1b and S4†).[38–40] As the conduction band minimum (CBM) of an n-type semiconductor is about 0.1 or 0.2 eV higher than the flat band potential, the CBMs of $CsPbBr_3$ QDs and $[Ni(dmgH)_2]$ are determined to be −1.09 eV and −0.69 eV, respectively. The valence band maximum (VBM) of $CsPbBr_3$ QDs is calculated to be 1.19 eV *vs.* NHE. Therefore, the Fermi level energy (E_f) of $CsPbBr_3$ QDs is high enough to transfer the photogenerated electrons from the CB of $CsPbBr_3$ to the LUMO of $[Ni(dmgH)_2]$ (Fig. 1c).[41]

Photoluminescence (PL) spectrum of $CsPbBr_3$ QDs showed the emission peak at 517 nm (Fig. 1d).[42] The emission peak intensity is gradually decreased with the increasing amount of cocatalyst as the introduction of $[Ni(dmgH)_2]$ into $CsPbBr_3$ solution significantly reduced the charge recombination process (Fig. 1d and S5†). In $[Ni(dmgH)_2]$, the strong π-acceptor conjugation in the ligand backbone facilitates the electron transfer from $CsPbBr_3$ QDs to the cocatalyst, minimizing the charge recombination process.[43] The trend in the PL intensity is also reflected in the photocatalytic C–N coupling reaction, where the best activity is observed with 7% [Ni]-$CsPbBr_3$ (Table S4†).

For a more comprehensive understanding, we recorded the PL of $[Ni(dmgH)_2]$ as well (Fig. S5†). PL reveals that $[Ni(dmgH)_2]$ has emission peaks at 507 nm and 562 nm.[38] A slight shift in the two fluorescence peaks was observed in 7% [Ni]-$CsPbBr_3$ compared to pure $[Ni(dmgH)_2]$, which can be attributed to the charge transfer from $CsPbBr_3$ QDs to the cocatalyst (Fig. S5†).

Further, the photocurrent response of the catalyst systems was recorded under on/off cycling of the light (Fig. 1e and S6†). Compared to $CsPbBr_3$ QDs, [Ni]-$CsPbBr_3$ photocatalysts showed a substantial improvement in the photocurrent density, and the best photocurrent response was achieved with 7% [Ni]-$CsPbBr_3$, indicating efficient separation of charges after cocatalyst addition. The $[Ni(dmgH)_2]$ captures the photogenerated electrons from $CsPbBr_3$ QDs, effectively minimizing charge recombination and enhancing the charge transfer.[42] The effective electron transfer was revealed through electrochemical impedance spectroscopy (EIS) measurements (Fig. S7†). The Nyquist plots of [Ni]-$CsPbBr_3$ exhibited noticeably smaller diameters in comparison to that of $CsPbBr_3$ QDs and 7% [Ni]-$CsPbBr_3$ showed the lowest charge-transfer resistance (R_{ct}) value (Fig. 1f).[44,45]

The HOMO–LUMO energy gap of the cocatalyst was determined using cyclic voltammetry (CV) and differential pulse voltammetry (DPV) in the presence of light and in the dark (Fig. 2a and S8†). In ground state, the energy gap between CB of $CsPbBr_3$ QDs and LUMO of $[Ni(dmgH)_2]$ is high. In the presence of light, the HOMO of $[Ni(dmgH)_2]$ shifts to a more positive potential value while the LUMO moves to a further negative potential. This leads to a reduction in the energy gap between the conduction band potential of $CsPbBr_3$ and the LUMO of $[Ni(dmgH)_2]$, facilitating the transfer of the photogenerated CB electrons to the cocatalyst. As a result, O_2 molecules are faster reduced to superoxide, improving the rate of photocatalytic C–N coupling reaction (see later).

The X-ray photoelectron spectroscopy (XPS) study has also shown strong electronic interaction between $CsPbBr_3$ QDs and

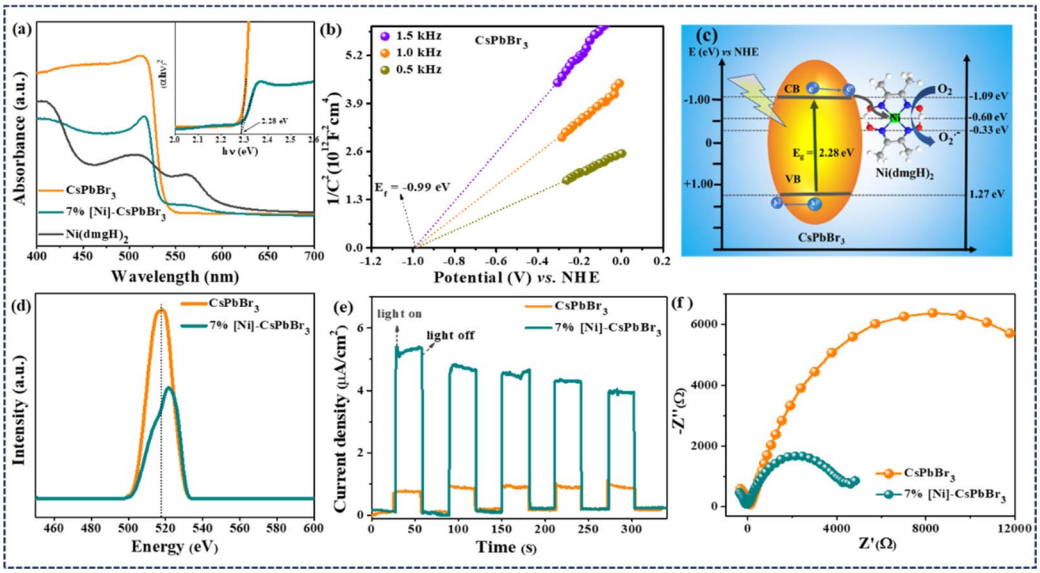

Fig. 1 (a) The UV-vis diffuse reflectance spectra of $CsPbBr_3$ QDs, 7% [Ni]-$CsPbBr_3$ and $[Ni(dmgH)_2]$, inset showing corresponding Tauc plot, demonstrating no significant change in the bandgap after the introduction of the cocatalyst to $CsPbBr_3$ QDs. (b) Mott–Schottky plot of $CsPbBr_3$ QDs. (c) Depiction of the conduction band minima and valence band maxima for $CsPbBr_3$ QDs and $[Ni(dmgH)_2]$, derived from Tauc plot and Mott–Schottky studies. (d) Photoluminescence spectra of $CsPbBr_3$ QDs and 7% [Ni]-$CsPbBr_3$ showing a reduction in the charge recombination process after the introduction of cocatalyst to $CsPbBr_3$ QDs. (e) Photocurrent measurements of $CsPbBr_3$ QDs and 7% [Ni]-$CsPbBr_3$ under light/dark conditions. (f) Electrochemical impedance spectroscopic studies of $CsPbBr_3$ QDs and 7% [Ni]-$CsPbBr_3$, revealing the low charge transfer resistance for 7% [Ni]-$CsPbBr_3$ (condition for recording photocurrent and EIS: electrolyte: 0.1 M $TBAPF_6$ in ethyl acetate (20 mL), photocatalyst@FTO: working electrode, Ag/AgCl: reference electrode, and Pt-wire: counter electrode; 0.0 V *vs.* Ag/AgCl was applied for photocurrent measurements. Light source: 15 W blue LED).

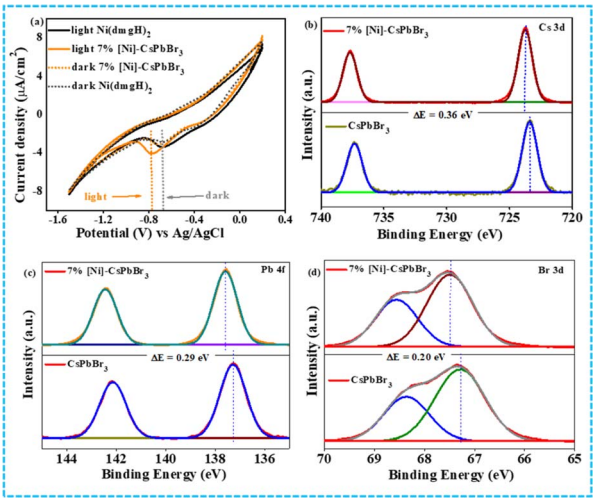

Fig. 2 (a) Cyclic voltammogram of $CsPbBr_3$ QDs and 7% [Ni]-$CsPbBr_3$ in the dark and light. XPS spectra of $CsPbBr_3$ and 7% [Ni]-$CsPbBr_3$ (b) Cs 3d, (c) Pb 4f, (d) Br 3d.

cocatalyst (Fig. 2b–d). The comparison of Cs 3d XPS of $CsPbBr_3$ QDs and 7% [Ni]-$CsPbBr_3$ showed a positive shift (0.33 eV) in the binding energies of Cs $3d_{5/2}$ (723.82 eV) and Cs $3d_{3/2}$ (737.79 eV) peaks after the cocatalyst incorporation, indicating electron transfer from the CB of photocatalyst to cocatalyst.

Similarly, Pb 4f and Br 3d XPS exhibited positive shifts in the binding energies in 7% [Ni]-$CsPbBr_3$ compared to that of $CsPbBr_3$. In contrast, a negative shift of Ni $2p_{3/2}$ and $2p_{1/2}$ peaks was detected in 7% [Ni]-$CsPbBr_3$ compared to that in $[Ni(dmgH)_2]$ due to the electron accumulation in the LUMO of the cocatalyst (Fig. S9†).[38] The C 1s, N 1s, and O 1s XPS spectra of 7% [Ni]-$CsPbBr_3$ are presented in Fig. S9.† Consequently, these findings provide strong evidence of electron transfer from $CsPbBr_3$ QDs to $[Ni(dmgH)_2]$.

Role of cocatalyst on photoredox activity

The optimization of the photoredox C–N coupling reaction was performed using 4-nitrobenzaldehyde (**1**) and piperidine (**2**) as the model substrates (Table S2†). $CsPbBr_3$ QDs produced amide by the photocatalytic reaction with a reduced yield (see later). However, the integration of the Ni-complex with $CsPbBr_3$ QDs significantly improved the photocatalytic activity (Table S2†). A series of Ni(II)-complexes and salts were explored as the cocatalyst {$[Ni(dmgH)_2]$, $[Ni(salen)_2]$, $[Ni(acac)_2]$, and $Ni(OAc)_2 \cdot 4H_2O$} with $CsPbBr_3$ QDs (Table S2†). Among different cocatalysts, $[Ni(dmgH)_2]$ was found to be the most effective for the photoredox C–N coupling reaction. The amount of cocatalyst has also a significant effect on the photoredox activity of [Ni]-$CsPbBr_3$ (Table S2†). With the increasing wt% of $[Ni(dmgH)_2]$, the photoredox activity was increased to achieve a higher yield of amide. Interestingly, the best yield of amide was obtained with 7% [Ni]-$CsPbBr_3$, and further increase in the amount of $[Ni(dmgH)_2]$ decreased the yield of the product (Table S2†).

Based on the above studies, it is clear that a cocatalyst should possess an optimized reduction potential and improve the

photogenerated charge separation and transport process of $CsPbBr_3$ QDs, enabling it to accept electrons from the $CsPbBr_3$ CB and relay the electron to atmospheric molecular oxygen (from air) to form superoxide radicals. It should be mentioned here that $CsPbBr_3$ QDs can also activate molecular oxygen to form superoxide radicals. However, the cocatalyst $[Ni(dmgH)_2]$ helps in the relay of the photogenerated electrons from the CB of $CsPbBr_3$ to O_2 because of the suitable energy levels and redox potentials.

To understand the process, we have conducted a comparison of the energy levels and reduction potentials of the three components: (i) CB position of $CsPbBr_3$ QDs, (ii) single electron reduction potential of $[Ni(dmgH)_2]$, and (iii) reduction potential of O_2 to $O_2^{\bullet-}$. The MS study confirms that the reduction potential of $[Ni(dmgH)_2]$ (-0.59 V *vs.* NHE) is higher enough to reduce O_2 to $O_2^{\bullet-}$ (-0.33 V *vs.* NHE) (Fig. 1c and S4†). As the superoxide radical is responsible for the activation of the aldehyde, the rate-determining step is not the initial photoexcitation or charge injection but the subsequent conversion of O_2 to $O_2^{\bullet-}$. Therefore, the optimized energy levels of the photocatalyst CB and cocatalyst LUMO can enhance the overall photoredox performance.

Optimization of the photoredox reaction conditions

Further optimization of the photoredox reaction conditions has been carried out in different aprotic solvents (tetrahydrofuran (THF), acetonitrile, toluene, and 1,4 di-oxane). Among these, THF was found to be the suitable solvent for the photoredox C–N bond formation. To understand the role of photocatalyst, cocatalyst, light, and O_2, photoredox reactions with all the necessary combinations have been performed (Table S2†). In the absence of photocatalyst or light, the reaction did not take place. In the N_2 environment (absence of O_2), a trace amount (<5%) of product formation was detected. This result clearly shows the importance of the activation of molecular oxygen to superoxide radicals for the photoredox reaction. However, in the absence of the cocatalyst, $CsPbBr_3$ QDs can also activate molecular O_2 and produce 48% yield of amide.

Substrate scope for the C–N bond formation

The C–N coupling strategy involving derivatives of benzaldehyde and piperidine demonstrated a wide substrate scope and remarkable tolerance to diverse functional groups, leading to the formation of amides in good to excellent yields (Table 1). The reactivity of aldehyde derivatives depends on the presence of electron-donating and electron-withdrawing groups in the phenyl ring of benzaldehydes. Substrates with the electron-donating group in the phenyl ring of benzaldehydes (*para*-methyl-benzaldehyde and *para*-methoxy benzaldehyde) showed comparatively low yields (Table 1, **3a–3c**). The steric crowding in the *ortho*-position of benzaldehyde further decreased the yield of the amide (Table 1, **3d**).

In contrast, benzaldehydes having electron-withdrawing groups (–NO_2, and –CF_3) in the phenyl ring produced high yields, ranging from 82% to 92% (Table 1, **3f–3i**). Further, the position of the substituent (*ortho*-, *meta*-, *para*-nitro) in the phenyl ring of benzaldehydes has shown a significant effect on the yield of the product (Table 1, **3f–3h**). Even, 4-bromobenzaldehyde produced a good yield of amide (89.5%) under the similar reaction conditions (Table 1, **3e**). The reaction of morpholine with different benzaldehyde derivatives produced slightly lower yield of amide than the corresponding piperidine derivative (Table 1, **3j–3l**).

The reaction of pyrrolidine with different substituted benzaldehydes produced a wide variety of amides (Table 1, **3m–3p**). A similar trend for the substitution in the phenyl ring of benzaldehyde was observed when 5-membered pyrrolidine was used instead of 6-membered piperidine. However, in all the cases, a slightly lower yield (74–89%) was attained with pyrrolidine compared to piperidine because of increased ring strain in the cationic amine radical of pyrrolidine (see later). Interestingly, the process can even tolerate hydroxyl group at the *ortho*-position of benzaldehyde to produce a yield of 56% of amide (Table 1, **3q**). The reaction of terephthaldehyde with pyrrolidine produced 69% yield of **3q** (Table 1, **3r**). The heterocyclic aldehydes (thiophene-2-carbaldehyde and pyridine 2-carbaldehyde) also produced >80% yield of amides (Table 1, **3s–3t**).

A wide variety of amines have also been studied to form amides with moderate to high yield. The effect of the variation of amine (with a similar structure) is not so pronounced in the yield of amides. For example, when 6-membered piperidine was replaced by morpholine, the yield was not significantly affected (Table 1, **3a**, and **3k**). Similarly, 6-membered piperidine and 5-membered pyrrolidine produced similar yields (Table 1, **3a**, and **3m**). However, the reaction of 2-oxolidone with benzaldehyde lowered the yield of the amide (Table 1, **3u**).

Interestingly, aniline derivatives of pyridine and quinoline (2-aminopyridine, 2-(2-pyridyl)ethylamine, and 7-aminoquinoline) also produced a high yield of amides when reacted with benzaldehyde (Table 1, **3v–x**). However, the reaction of aniline with benzaldehyde led to the formation of a mixture of products, which cannot be separated by column chromatography. Even benzylamine produced 72% yield of amide reacting with benzaldehyde (Table 1, **3y**). However, the yield of the amide was decreased when aliphatic aldehyde was reacted with benzylamine (Table 1, **3z**). Octanal showed only 61% conversion under similar reaction conditions with a 55% yield of amide and 6% yield of *N*-octylidene-1-phenylmethanamine as a byproduct following the hydrogen atom transfer (HAT) mechanism (Table S5,† **3z′**).[46] A decrease in the yield of amides was also observed when benzaldehyde reacted with open-chain aliphatic amines (Table 1, **3aa**, and **3bb**).

Further, the catalytic recyclability test was performed four times with a minimum loss of activity (Fig. S10†). The recovered catalyst did not show any change in the UV-visible spectrum (Fig. S11†).

Effect of cocatalyst on the excited state dynamics of $CsPbBr_3$ QDs

The femtosecond transient absorption spectroscopy (TAS) was used to investigate the impact of $[Ni(dmgH)_2]$ on the dynamics of carrier relaxation in $CsPbBr_3$ QDs (Fig. S12†). The samples

Table 1 Photocatalytic C–N bond formation in the presence of visible light using 7% [Ni]-$CsPbBr_3$ photocatalyst[a]

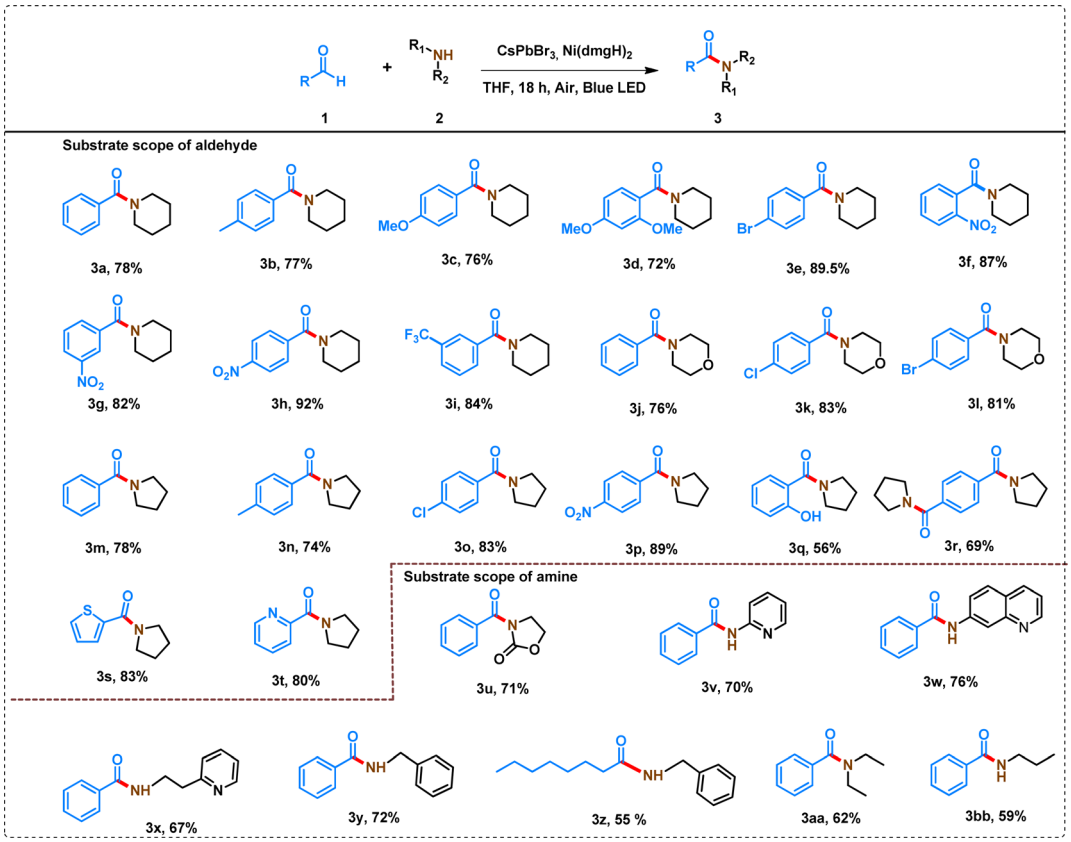

[a] Reaction conditions: aldehyde (0.5 mmol), amine (1 mmol), 7% [Ni]-$CsPbBr_3$ (10 mg), THF (2.5 mL), 15 W blue LED, air, temperature: 35 ± 3 °C, time: 18 h. *In the case of **3r**, aldehyde and pyrrolidine were taken 0.5 mmol and 2 mmol, respectively. In all the cases, isolated yield of the product was reported and the products were characterized by ^1H and ^{13}C NMR (Table S5).

were excited above the band edge of $CsPbBr_3$ (370 nm) to generate charge carriers, which subsequently formed trap states.[34,35] The TAS of $CsPbBr_3$ reveals specific features (Fig. S12a–g†): (i) a prominent photobleach band at 518 nm (PB1). (ii) A less pronounced negative band (390–450 nm: PB2). (iii) A broad absorption band (410–510 nm: ESA1). (iv) Another excited state absorption band (530–560 nm: ESA2). This second absorption band evolves and decays rapidly within 800 fs. A concomitant broadening and a red shift of ESA1 are observed within this time scale. The ESA2 is ascribed to the intra-band relaxation of the hot electron in the vibrational levels of the conduction bands of $CsPbBr_3$.[35] As the relaxation takes place, the energy gap between the relaxed states and higher energy states increases which leads to a blue shift of the ESA2. This overlaps with the wavelengths of ESA1 and appears to broaden and enhance the intensity of ESA1.

The TA of 7% [Ni]-$CsPbBr_3$ showed similar spectral features for the photobleach bands and the lower wavelength ESA band (PB3, PB4, and ESA3) (Fig. S12h–n†). The excited absorption band, akin to ESA2 in $CsPbBr_3$, was not detected in 7% [Ni]-$CsPbBr_3$. Photo-induced absorption ESA3 appeared at 510 nm while the photo bleach band PB3 was red-shifted (526 nm) compared to that of $CsPbBr_3$ (Fig. S12h–n†). Although several spectral features were observed to be similar in QDs and 7% [Ni]-$CsPbBr_3$, the rates at which the spectra evolve are significantly different. This suggests that the same electronic states are involved but their formation rates are different.

The decay dynamics at different wavelengths are monitored by fitting the kinetic traces to a sum of exponentials. The kinetic trace at 400 nm corresponds to the bleach of the ground state to the higher energy states (Fig. 3a(1)). The 550 nm kinetics belongs to the recovery of bleach of ground state as this wavelength matches the lowest energy band in the steady state spectrum. A negative signal in the TA can be assigned to bleach as well as stimulated emission. The hot electrons undergo intra-band relaxation processes. Had the signal at 390 nm to 430 nm been exclusively from the stimulated emission of hot electrons, then this band would have evolved along with ESA2. However, as noted from TA spectra (Fig. S12†) this blue band exists well beyond ESA2 absorption. ESA2 rises and falls within 800 fs, while the PB2 signatures exist even in the 2 ns spectra. The 7% [Ni]-$CsPbBr_3$ spectra also showed the negative band in the same region, however, the ESA2-type band was not observed. Based on the electrochemical spectroscopic studies, an ultrafast electron transfer from perovskite to cocatalyst can be proposed. If the negative band is originated from the stimulated emission of hot electrons, it should not be detected in 7% [Ni]-$CsPbBr_3$. As

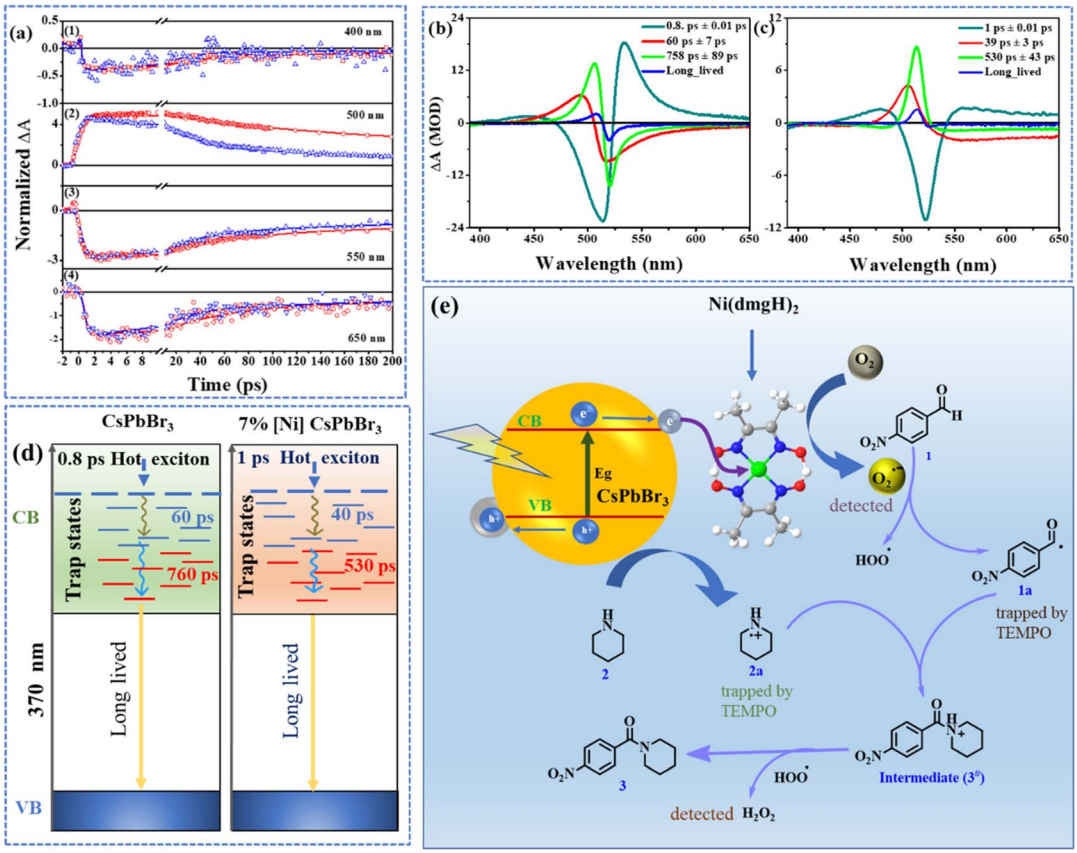

Fig. 3 (a) Kinetic traces at (1) 400 nm (2) 500 nm (3) 550 nm and (4) 650 nm for $CsPbBr_3$ (red) and 7% [Ni]-$CsPbBr_3$ (blue). The solid lines are fitted lines. The decay-associated spectra (DAS) of (b) $CsPbBr_3$ and (c) 7% [Ni]-$CsPbBr_3$. (d) Schematic illustration of the formation and relaxation of charge carriers of $CsPbBr_3$ and 7% [Ni]-$CsPbBr_3$. (e) Proposed mechanism of C–N bond formation.

the higher energy negative band was detected even in the presence of cocatalyst, we assigned it as a photobleach band.

The comparison of the kinetic traces at 500 nm has shown that the rise and decay of the signal of $CsPbBr_3$ is faster than 7% [Ni]-$CsPbBr_3$ (Fig. 3a(2)). The rise times were calculated to be 98 ± 5 ps for $CsPbBr_3$ and 41 ± 2 ps for 7% [Ni]-$CsPbBr_3$. The recovery of bleach (550 nm) was found to be faster for 7% [Ni]-$CsPbBr_3$ than pristine QDs (Fig. 3a(3)). The same inference was drawn from 400 nm traces as well. The lifetimes at 550 nm decreased from 60 ± 8 ps and 817 ± 165 ps for $CsPbBr_3$ to 31 ± 3 ps and 293 ± 32 ps for 7% [Ni]-$CsPbBr_3$. Similar observations were obtained for kinetic traces at 650 nm (Fig. 3a(4)) and the time constants are listed in Table S3.† The decay-associated spectra (DAS) revealed three ultrafast components for both systems (Fig. 3b and c).[47] The global lifetimes are obtained as 0.8 ± 0.01 ps, 60 ± 7 ps, and 758 ± 89 ps for $CsPbBr_3$ and 1 ± 0.01 ps, 39 ± 3 ps, and 530 ± 43 ps for 7% [Ni]-$CsPbBr_3$.

In addition to the above three components, a long-lived component, associated with the charge recombination process, that did not decay within the timescale of our measurement, was also observed (Fig. S13†). The DAS at 0.8 ± 0.01 ps showed a strong positive band (533 nm) corresponding to ESA2. The strong positive band in the DAS at 60 ± 7 ps matched with ESA1. The amplitude at the peak of ESA1 of the 760 ps DAS is stronger than that observed in the 60 ps DAS. This is in line with the observation that the ESA1 becomes stronger over the range of 500 ps and then decays. The DAS has a longer lifetime having a positive band at the same wavelength 506 nm associated with the ESA1 and PB1 bands (Fig. S12†). PB1 is attributed to the depopulation of the ground state, as its peak position aligns with the lowest energy steady-state absorption of the $CsPbBr_3$ (Fig. S12a†).[48,49] The 0.8 ps rise in PB1 signal resulting from 370 nm excitation is attributed to the gradual transition of the high energy excitons towards the band edge excitonic state through intra-band relaxation.

The loading of $[Ni(dmgH)_2]$ on $CsPbBr_3$ results in faster kinetics in the TAS (Fig. 3d). A faster decay arises from the increased rate of depopulation of the involved states by an excited state process due to the migration of the charge from $CsPbBr_3$ to $[Ni(dmgH)_2]$. This is manifested as a decrease in lifetime in 7% [Ni]-$CsPbBr_3$ and is a reflection of the formation of a trap state from $CsPbBr_3$. Earlier works on $CsPbBr_3$ have also indicated that the exciton bleach in the picosecond to nanosecond time scales serves as a reliable indicator of electron trapping.[48,50,51]

The electrochemical studies showed that light-induced charge transfer was facilitated from $CsPbBr_3$ to $[Ni(dmgH)_2]$ (Fig. 2a and S8†). We take the aid of TA measurements to

estimate the rate of this migration. The lifetimes of exciton formation and cooling are affected by cocatalyst. The inverse of lifetime corresponds to the rate constant of the associated process. Hence the difference in rate constants of $[Ni(dmgH)_2]$ loaded and pristine $CsPbBr_3$ will serve as a measure of the electron transfer process (eqn S1†). The formation time of the trap state decreases from 60 ± 8 ps for $CsPbBr_3$ to 31 ± 3 ps for 7% [Ni]-$CsPbBr_3$. Substituting these lifetimes yields a rate constant of $k_{et} = 1.6 \times 10^{10}$ s^{-1}. The observed electron transfer rate agrees with the rate constant typically observed in other semiconductor metal systems where electrons have relaxed to the bottom of the conduction band.[51,52]

Reaction mechanism

The reaction of 4-nitrobezaldehyde and piperidine in the inert atmosphere resulted <5% product formation, highlighting the role of oxygen. Furthermore, when we introduced electron and hole scavengers ($AgNO_3$ and TEA or ethanol) into the reaction mixture, the yield of the product decreased significantly, suggesting the involvement of free-radical pathways (Fig. S14†). When superoxide radical scavenger *para*-benzoquinone was introduced into the reaction mixture, the yield of the product dropped to only 10% (Fig. S14†).[16]

In the presence of $[Ni(dmgH)_2]$, faster electron transfer from the CB of $CsPbBr_3$ to cocatalyst takes place, followed by the reduction of surface-bound O_2, producing superoxide radicals. Considering these findings, we have proposed a mechanism for the photo-induced amide formation reaction (Fig. 3e). Under visible light irradiation, [Ni]-$CsPbBr_3$ is initially photoexcited, promoting an electron from the VB to CB. This photogenerated electron in the CB is relayed to atmospheric oxygen by cocatalyst to form a superoxide radical ($O_2^{\bullet -}$). Concurrently, the holes (h^+) in the VB are transferred to amine (**2**), resulting in the formation of amine radical cation (**2a**). The superoxide radical abstract proton from 4-nitrobenzaldehyde forms acyl radical (**1a**) along with a hydroperoxyl radical ($^{\bullet}OOH$).[26,53–58] Interestingly, intermediate **1a** and **2a** were trapped by TEMPO and identified using NMR spectroscopy (Fig. S15a†) and mass spectrometry (Fig. S15b†).[59] The radical coupling of intermediates **1a** and **2a** produces cationic species $3^{\#}$, which is further oxidized by $^{\bullet}OOH$ to final product **3**.[53,54] As a result, H_2O_2 was formed as the reduction product of O_2. Interestingly, we were able to detect the formation of H_2O_2 (Fig. S16†).[60,61]

The higher efficiency of O_2 reduction by 7% [Ni]-$CsPbBr_3$ compared to $CsPbBr_3$ was also confirmed (Fig. S16a†). Further, an increase in H_2O_2 concentration was observed with increasing reaction time (Fig. S16b†). Therefore, it is clear that 7% [Ni]-$CsPbBr_3$ is more effective in the activation of molecular oxygen compared to $CsPbBr_3$. In addition, superoxide radical was also detected by UV-visible spectroscopy (Fig. S17†).[62,63] A higher amount of $O_2^{\bullet -}$ formation was also observed for 7% [Ni]-$CsPbBr_3$ compared to the pristine QDs.

Therefore, in this study, we are able to detect the reaction intermediates (**1a**, **2a**) by mass-spectroscopy and NMR, active radical spices ($O_2^{\bullet -}$) and H_2O_2 by UV-visible spectroscopy (Fig. S15–S17†). Based on the previous literature, the formation of $^{\bullet}OOH$ radicals and $3^{\#}$ has been proposed to complete the catalytic cycle.[60–63]

Conclusion

In summary, we have demonstrated the potential of $CsPbBr_3$ QDs for the photoredox C–N coupling reaction. The introduction of cocatalyst improved the photoredox process and the best catalytic activity was obtained with $[Ni(dmgH)_2]$ because of the suitable band alignment. $[Ni(dmgH)_2]$ enhances photogenerated charge transfer dynamics of $CsPbBr_3$ QDs. 7% [Ni]-$CsPbBr_3$ produced the best photoredox activity forming amide with 92% yield. Ultrafast TA measurement showed that electron transfer to $[Ni(dmgH)_2]$ originated from $CsPbBr_3$, exhibiting a rate constant of $k_{et} = 1.6 \times 10^{10}$ s^{-1}. The trap states decayed significantly fast, thereby enhancing the photocatalytic activities. Importantly, the optimal reaction conditions for these transformations avoid non-oxygen oxidants, harsh reaction conditions, ligands, additives, and environmentally hazardous solvents and bases. This study has shown the potential of photoredox reactions using semiconductor QDs for the synthesis of valuable compounds.

Data availability

All the data are available in the ESI.†

Author contributions

VK involved in the synthesis of the catalysts, their characterization, photocatalytic studies, data interpretation, and manuscript writing. VV involved in product separation (column chromatography) and NMR. DK carried out (photo)electrochemical characterization and data interpretation. SKP and ESSI conducted transient absorption measurements and wrote their part. The project design, conceptualization, supervision, data interpretation, manuscript writing, and editing were performed by AI.

Conflicts of interest

There are no conflicts to declare.

Acknowledgements

AI would like to thank DST-SERB, India for the core research grant (Grant No.: CRG/2023/002395). VK is thankful to CSIR [09/1217/(0084)/2020-EMR-II] for providing the senior research fellowship.

Notes and references

1 C. Russo, F. Brunelli, G. C. Tron and M. Giustiniano, *J. Org. Chem.*, 2023, **88**, 6284–6293.
2 G. E. M. Crisenza and P. Melchiorre, *Nat. Commun.*, 2020, **11**, 803.

3 H. Huang, B. Pradhan, J. Hofkens, M. B. J. Roeffaers and J. A. Steele, *ACS Energy Lett.*, 2020, **5**, 1107–1123.
4 D. Sun, Y. Chen, X. Yu, Y. Yin and G. Tian, *Chem. Eng. J.*, 2023, **462**, 142084.
5 P. Sha, L. Huang, J. Zhao, Z. Wu, Q. Wang, L. Li, D. Bu and S. Huang, *ACS Catal.*, 2023, **13**, 10474–10486.
6 A. Wang, M. Du, J. Ni, D. Liu, Y. Pan, X. Liang, D. Liu, J. Ma, J. Wang and W. Wang, *Nat. Commun.*, 2023, **14**, 6733.
7 Y. Zheng, Y. Chen, B. Gao, B. Lin and X. Wang, *Adv. Funct. Mater.*, 2020, **30**, 2002021.
8 A. Indra, R. Beltrán-Suito, M. Müller, R. P. Sivasankaran, M. Schwarze, A. Acharjya, B. Pradhan, J. Hofkens, A. Brückner, A. Thomas, P. W. Menezes and M. Driess, *ChemSusChem*, 2021, **14**, 306–312.
9 A. Indra, P. W. Menezes, M. Schwarze and M. Driess, *New J. Chem.*, 2014, **38**, 1942–1945.
10 A. Indra, P. W. Menezes, K. Kailasam, D. Hollmann, M. Schröder, A. Thomas, A. Brückner and M. Driess, *Chem. Commun.*, 2016, **52**, 104–107.
11 S. Alemdar, A. Basak and O. Metin, *ACS Appl. Mater. Interfaces*, 2023, **15**, 48096–48109.
12 A. P. Deshmukh, K. Patil, S. Ogale and T. Bhave, *ACS Appl. Electron. Mater.*, 2023, **5**, 1536–1545.
13 H. Kasap, C. A. Caputo, B. C. M. Martindale, R. Godin, V. W. H. Lau, B. V. Lotsch, J. R. Durrant and E. Reisner, *J. Am. Chem. Soc.*, 2016, **138**, 9183–9192.
14 H. Jiang, M. Liu, X. Lian, M. Zhu and F. Zhang, *Angew. Chem., Int. Ed.*, 2024, **136**, e202318850.
15 I. Rosa-Pardo, C. Casadevall, L. Schmidt, M. Claros, R. E. Galian, J. Lloret-Fillol and J. P. Prieto, *Chem. Commun.*, 2020, **56**, 5026–5029.
16 Q. Fan, H. Zhang, D. Liu, C. Yan, H. Zhu, Z. Xie and Z. Le, *J. Org. Chem.*, 2023, **88**, 7391–7400.
17 J. Lee, A. Kumar and H. Tuysuz, *Angew. Chem., Int. Ed.*, 2024, 202404496.
18 K. Mishra, D. Guyon, J. San Martin and Y. Yan, *J. Am. Chem. Soc.*, 2023, **145**, 17242–17252.
19 Y. Dong, Y. Feng, Z. Li, H. Zhou, H. Lv and G. Y. Yang, *ACS Catal.*, 2023, **13**, 14346–14355.
20 X. Zhu, Y. Lin, Y. Sun, M. C. Beard and Y. Yan, *J. Am. Chem. Soc.*, 2019, **141**, 733–738.
21 X. Zhu, Y. Lin, J. San Martin, Y. Sun, D. Zhu and Y. Yan, *Nat. Commun.*, 2019, **10**, 2843.
22 K. Chen, X. Deng and G. Dodekatos, *J. Am. Chem. Soc.*, 2017, **139**, 12267–12273.
23 Y. Yuan, H. Zhu, K. H. Kimball, T. Cai, W. Shi, Z. Wei, H. Yang, Y. Candler, P. Wang, J. He and O. Chen, *Angew. Chem., Int. Ed.*, 2020, **59**, 22563–22569.
24 J. S. Martin, X. Zeng, X. Chen, C. Miller, C. Han, Y. Lin, N. Yamamoto, X. Wang, S. Yazdi, Y. Yan, M. C. Beard and Y. Yan, *J. Am. Chem. Soc.*, 2021, **143**, 11361–11369.
25 W. Wu, Y. C. Wong, Z. K. Tan and J. Wu, *Catal. Sci. Technol.*, 2018, **8**, 4257–4263.
26 L. Xu, S. Z. Zhang, W. Li and Z. H. Zhang, *Chem.–Eur. J.*, 2021, **27**, 5483–5491.
27 L. Deng, L. Chen, L. Zhu, Y. Li, J. Ou-Yang, S. Wu, P. Chen, S. Shen, J. Guo, Y. Zhou, C. T. Au and S. F. Yin, *Chem. Eng. Sci.*, 2022, **261**, 117960.
28 B. Goel, V. Vyas, N. Tripathi, A. K. Singh, P. W. Menezes, A. Indra and S. K. Jain, *ChemCatChem*, 2020, **12**, 5743–5749.
29 V. Vyas, V. Kumar and A. Indra, *Chem. Commun.*, 2024, **60**, 2544–2547.
30 O. G. Mountanea, D. Psathopoulou, C. Mantzourani, M. G. Kokotou, E. A. Routsi, D. Tzeli, C. G. Kokotos and G. Kokotos, *Chem.–Eur. J.*, 2023, **29**, 2300556.
31 N. Martín and F. G. Cirujano, *Catal. Commun.*, 2022, **164**, 106420.
32 A. Hassan Tolba, M. Krupička, J. Chudoba and R. Cibulka, *Org. Lett.*, 2021, **23**, 6825–6830.
33 Y. C. Pu, Y. H. Chuang, M. W. Zheng, Y. J. Chang and S. H. Liu, *J. Environ. Chem. Eng.*, 2023, **11**, 109103.
34 H. Wang, W. Lu, P. Xu, J. Luo, K. Yao, J. Zhang, X. Wei, S. Peng, H. Cheng, H. Hu and K. Sun, *ACS Sustain. Chem. Eng.*, 2023, **11**, 5963–5972.
35 J. Ding, X. Deng, J. Fan, Y. Wang, Z. Li and Q. Liang, *Inorg. Chem.*, 2023, **62**, 16493–16502.
36 X. Deng, Q. Liang, J. Fan, X. Yan, H. Si, H. Huang, Z. Li and Z. Kang, *Chem. Eng. J.*, 2023, **475**, 146385.
37 F. Xu, K. Meng, B. Cheng, S. Wang, J. Xu and J. Yu, *Nat. Commun.*, 2020, **11**, 14613.
38 S. Liu, F. Li, T. Li and W. Cao, *J. Colloid Interface Sci.*, 2023, **642**, 100–111.
39 Z. Zhang, L. Li, Y. Jiang and J. Xu, *Inorg. Chem.*, 2022, **61**, 3351–3360.
40 J. Ma, W. Meng, L. Zhang, F. Li and T. Li, *RSC Adv.*, 2021, **11**, 5035–5043.
41 Y. Zhang, L. Shi, H. Yuan, X. Sun, X. Li, L. Duan, Q. Li, Z. Huang, X. Ban and D. Zhang, *Chem. Eng. J.*, 2022, **430**, 132820.
42 Z. Chen, Y. Hu, J. Wang, Q. Shen, Y. Zhang, C. Ding, Y. Bai, G. Jiang, Z. Li and N. Gaponik, *Chem. Mater.*, 2020, **32**, 1517–1525.
43 S. Y. Ali, K. D. Reddy and A. K. Manna, *J. Phys. Chem. A*, 2019, **123**, 9166–9174.
44 Y. F. Xu, M. Z. Yang, H. Y. Chen, J. F. Liao, X. D. Wang and D. Bin Kuang, *ACS Appl. Energy Mater.*, 2018, **1**, 5083–5089.
45 W. Gong, Y. Li, Y. Yang, H. Guo and X. Niu, *J. Mater. Chem. C*, 2023, **11**, 6963–6970.
46 A. J. McMillan, M. Sieńkowska, P. Di Lorenzo, G. K. Gransbury, N. F. Chilton, M. Salamone, A. Ruffoni, M. Bietti and D. Leonori, *Angew. Chem., Int. Ed.*, 2021, **133**, 7208–7215.
47 I. H. M. Van Stokkum, D. S. Larsen and R. Van Grondelle, *Biochim. Biophys. Acta, Bioenerg.*, 2004, **1657**, 82–104.
48 K. Wu, G. Liang, Q. Shang, Y. Ren, D. Kong and T. Lian, *J. Am. Chem. Soc.*, 2015, **137**, 12792–12795.
49 F. Deschler, M. Price, S. Pathak, L. E. Klintberg, D. D. Jarausch, R. Higler, S. Hüttner, T. Leijtens, S. D. Stranks, H. J. Snaith, M. Atatüre, R. T. Phillips and R. H. Friend, *J. Phys. Chem. Lett.*, 2014, **5**, 1421–1426.
50 C. Harris and P. V. Kamat, *ACS Nano*, 2010, **4**, 7321–7330.

51 K. Wu, H. Zhu, Z. Liu, W. Rodr and T. Lian, *J. Am. Chem. Soc.*, 2012, 10337–10340.
52 G. Nanoparticles, W. Virginia and U. States, *J. Phys. Chem. Lett.*, 2011, **2**, 2125–2129.
53 Z. Akrami and M. Hosseini-Sarvari, *Eur. J. Org. Chem.*, 2022, 202200429.
54 A. Dey, S. Chakraborty, A. Singh, F. A. Rahimi, S. Biswas, T. Mandal and T. K. Maji, *Angew. Chem., Int. Ed.*, 2024, e202403093.
55 F. K. C. Leung, J. F. Cui, T. W. Hui, K. K. Y. Kung and M. K. Wong, *Asian J. Org. Chem.*, 2015, **4**, 533–536.
56 L. Deng, L. Chen, L. Zhu, Y. Li, J. Ou-Yang, S. Wu, P. Chen, S. Shen, J. Guo, Y. Zhou and C. T. Au, *Chem. Eng. Sci.*, 2022, **261**, 117960.
57 D. Leow, *Org. Lett.*, 2014, **16**, 5812–5815.
58 A. Banerjee, Z. Ley and M. Y. Ngai, *Synthesis*, 2019, **51**, 303–333.
59 L. Wang, M. Yu, C. Wu, N. Deng, C. Wang, X. Yao and A. Syn, *Catal.*, 2016, **358**, 2631–2641.
60 L. Magerusan, C. Socaci, F. Pogacean, M. C. Rosu, A. R. Biris, M. Coros, A. Turza, V. Floare-Avram, G. Katona and S. Pruneanu, *RSC Adv.*, 2016, **6**, 79497–79506.
61 A. K. Singh, D. Hollmann, M. Schwarze, C. Panda, B. Singh, P. W. Menezes and A. Indra, *Adv. Sustainable Syst.*, 2021, **5**, 2000288.
62 J. Luo, X. Wei, Y. Qiao, C. Wu, L. Li, L. Chen and Ji. Shi, *Adv. Mater.*, 2023, **35**, 2210110.
63 A. K. Singh, K. Bijalwan, N. Kaushal, A. Kumari, A. Saha and A. Indra, *ACS Appl. Nano Mater.*, 2023, **6**, 8036–8045.